Multi-material, multi-process, planar and nonplanar additive manufacturing of piezoelectric devices

Mohammad Rafiee, Floriane Granier, Rui Tao, Abraham Bhérer-Constant, Gabriel Chenier and Daniel Therriault†*

Department of Mechanical Engineering, Polytechnique Montreal, Montreal, QC H3T 1J4, Canada

ABSTRACT

Nonplanar multi-material additive manufacturing (AM) of piezoelectric devices is an important step for innovation in digital manufacturing. In this work, we report the development of a manufacturing platform based on multi-material multi-process AM that enables fabrication of piezoelectric and conductive electrode materials with complex planar and nonplanar (conformal) structures. We also present the development of conductive and piezoelectric paste-like printing materials, herein called inks, for extrusion-based direct-writing additive manufacturing processes. Our developed inks are highly stretchable (e.g., up to 100% before breaking), easy to process, less toxic compared to existing solvent evaporation-based inks in the literature. We fabricated several piezoelectric energy harvesting (PEH) devices. Our innovative inks within a multi-material multi-process 3D printing platform can substantially broaden the design space of multi-material AM and open up new opportunities for the production of application-oriented parts that are more integrable, conformable, scalable, and versatile.

* mrafiee20@gmail.com

† daniel.therriault@polymtl.ca

Keywords: additive manufacturing, nonplanar 3D printing, piezoelectric materials, conductive inks, multi-material 3D printing, direct ink writing, fused filament fabrication

1. Introduction

The multi-material extrusion-based additive manufacturing (AM) can enhance the performance of manufactured parts by adding more shape complexity and functionality[1]. Although traditional extrusion-based multi-material AM is extensively customizable, it is often limited in functionality of the printed parts due to limitation in using only one type of AM process such as fused filament fabrication (FFF) or direct ink writing (DIW) within a single machine[2,3]. Another limitation consists of only a planar approach in building the desired models by slicing a 3D model into a large set of parallel planar layers. Envisioning an evolution for AM, the ensuing step involves developing non-planar layer-based processes and improvement of the functionality of additively manufactured components via more integrated multi-process AM that combines two or more AM processes. By using motion in all three x, y and z spatial dimensions during the deposition of each layer, regardless of layer height, non-planar layers better represent freeform surfaces than planar layers. The ability to create end-use products that contain complete circuits, sensors, optics, and other components and freeform surfaces without sacrificing the geometric benefits of AM parts is a transformative approach in digital manufacturing [1,3,4].

Piezoelectric materials convert mechanical into electrical energy and vice versa, and have a variety of applications from actuation and pressure sensing to piezoelectric energy harvesting[5–7]. In recent years, the AM of some components of piezoelectric devices has been demonstrated [8–13]. Being self-powered further renders piezoelectric materials promising for remote location devices, human body organs, and inaccessible or confined spaces[14,15]. Although, AM of such devices is realized successfully using variety of techniques, some concerns regarding the availability and performance of materials being used for both the

piezoelectric and the conductive electrode components[14]. These works are also generally limited to very simple geometries and/or suffer from multi-step manufacturing that involves the fabrication of piezoelectric layer and the conductive electrodes using different manufacturing platforms[15].

So far, a few research works have been conducted to design stretchable piezoelectric and stretchable conductive inks with characteristics such as low manufacturing cost, environmentally sustainable production method, recyclability, lightweight, low energy consumption, and ease of integration in multi-material structures[16,17]. While conductive inks received the most attention[17–21], there is little research on the development of stretchable piezoelectric inks[17,22,23]. The inks developed in the literature are often designed for fabrication methods other than 3D printing (e.g., screen printing) and require extra heat curing step [8,18,24], and/or high content of toxic solvents [9,18]. Additionally, complex steps involving multi-process approaches are needed to fabricate a device, which limit the scalability and facile manufacturing.

Herein, we report the design of new conductive and piezoelectric inks compatible with a manufacturing platform based on multi-material multi-process AM for the creation of complex planar and nonplanar piezoelectric and conductive structures. Specifically, we combined DIW with FFF within a single manufacturing platform to fabricate flexible and stretchable piezoelectric energy harvesting (PEH) devices (Figure S1). In this AM platform, two printheads are equipped with a dispensing apparatus for DIW and one printhead is mounted with an FFF thermoplastic filament liquefier. We 3D printed several piezoelectric demonstrators and studied their piezoelectric properties and energy harvesting performance. The experimental results showed that the fabricated piezoelectric devices possess significant piezoelectric properties for sensing and energy harvesting applications. Such materials and

manufacturing development could be further employed as a fascinating tool that enables the production of various innovative material systems.

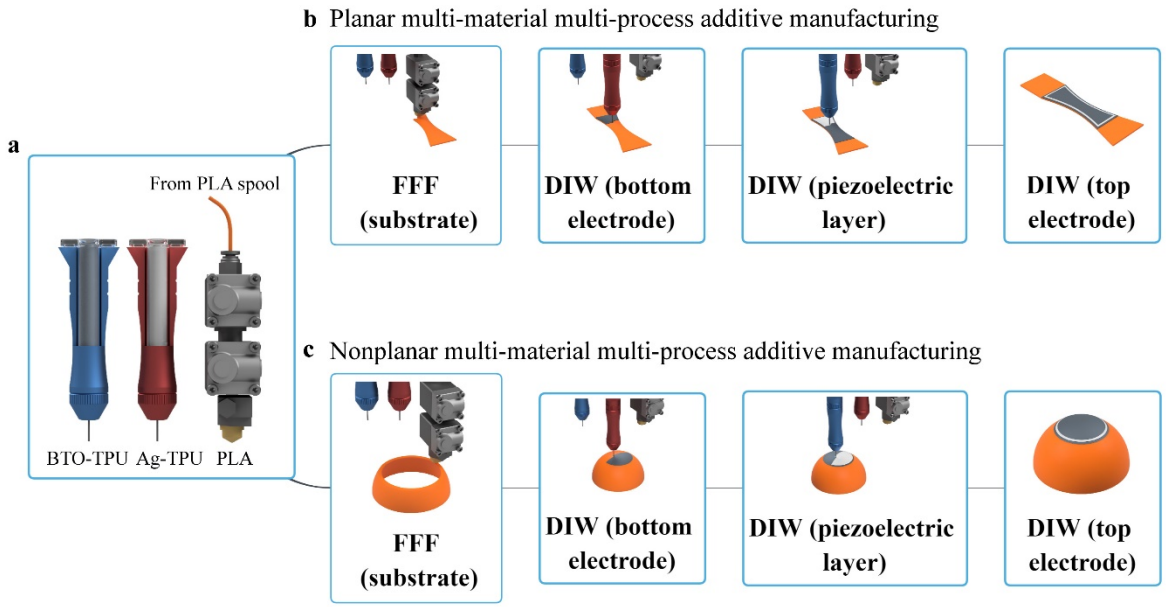

Figure 1. Schematic of multi-material multi-process planar and nonplanar additive manufacturing of piezoelectric devices: **a** schematic of DIW and FFF printing heads containing Ag-TPU, BTO-TPU inks and PLA filament, **b** schematic of planar AM of a multi-layer piezoelectric device with varying cross-section, **c** schematic of nonplanar AM of a semi-spherical shell piezoelectric demonstrator.

2. Results

2.1 Planar and nonplanar additive manufacturing set-up and ink formulation

To fabricate PEH devices, we first designed piezoelectric and highly conductive electrode inks using a thermoplastic polyurethane (TPU) matrix that embody the required rheological properties for DIW 3D printing process. Unlike prior ink designs that require extra heat curing step [8,18,24], and/or high content of toxic solvents [9,18], our piezoelectric and

conductive electrode inks are less toxic (with respect to existing inks in the literature[9,18]) and do not require heat cure after printing while exhibiting adequate viscosity (not too low to affect the formation of deposited filaments and not too high to make it impossible to push the material through the nozzle) desired for DIW. Specifically, we formulated the inks using TPU as the matrix, silver flakes and barium titanate ($BaTiO_3$ also namely called BTO) as the conductive and piezoelectric fillers, and Dimethylformamide (DMF) and Acetone as the co-solvent system. We used BTO for their large electro-mechanical coupling coefficient, excellent dipole moment, and large dielectric constant in TPU matrix to achieve high piezoelectric properties. Being environmentally friendly and easy handling as a lead-free material also made BTO our preferred material [25].

In DIW, the inks should be able to be extruded smoothly through dispensing nozzles (cone or cylindrical) and be able to be rapidly support itself soon after deposition, to keep the deposited material shape (Figure 2a). Shear rate of printing rheology shows the ink extruding capability from the nozzle. To limit evaporation of solvent, we use a solvent trap during the measurement. As shown in Figure S2, a shear-thinning behavior can be observed in both Ag-TPU and BTO-TPU inks. The apparent printing shear rate is a process parameters dependent and can be approximately calculated by $4V/(\pi r)$, where r is the nozzle radius, and V is the printing speed [26]. In our work (nozzle diameter of 250 μm and printing speed of 10 mm s^{-1}), the estimated printing shear rate is 50 s^{-1}.

Ink conductivity

The experimental data for the resistivity and conductivity of the Ag-TPU films at 0% strain as a function of silver flakes volume fractions is shown in Figure 2b with black and red triangle symbols, respectively. The conductivity of the silver film was theoretical predicted using 3D percolation theory and a power-law relationship described by $\sigma = \sigma_0 (V_f - V_c)^s$. In this

prediction, σ and σ_0 are the electrical conductivity of the silver film, and the conductivity of the silver flakes, respectively. V_f and V_c are the volume fraction of the dried silver flakes, and the volume fraction (in dried form) at the percolation threshold. In the relationship, s is the power law fitting exponent. The calculated percolation threshold and the power law fitting exponent ($V_c \approx 0.08$ and $s \approx 0.911$) indicated good agreement with our experimental results. Because of their anisotropic behavior, alignment of silver flakes (Figure 3b) due to shear forces within the Ag-TPU ink is expected during deposition. Based on the obtained data, Ag-TPU inks composed of 55 vol. % Ag was chosen to work with, which exhibit an initial conductivity above 1.87×10^5 S/m desired for high voltage poling and sensing applications.

It should be noted that extruding inks smoothly through dispensing nozzles is one of the limiting factors for maximum volume fraction of fillers in the TPU matrix. For instance, conductive ink with volume fraction higher than 70% by volume were not printable. Similarly, BTO-TPU ink were not printable at high content above 70% and we chose to go with 40% due to its optimum printability and adequate performance for our demonstrators.

Figure 2**c** shows the resistivity of the Ag-TPU films (55 vol. % Ag, dimensions: $40 \times 10 \times 0.17\ mm^3$) measured under different tensile strains using four-probe electrical conductivity measurement method. The as-prepared silver films show a maximum resistivity of ~ 1.61, 2.74 and 4.90 Ω at 10, 20, and 30% strain, respectively. The resistivities of the silver films were however, reduced with unloading the strain to around 1 Ω. Mechanical hysteresis of TPUs are believed to be reason for these distinctive unloading curves [27].

Stretchability of inks. Tensile properties of both Ag-TPU and BTO-TPU films were obtained using a universal testing machine and the results are shown in Figure 2**d.** The tensile results indicate that the developed conductive and piezoelectric films exhibit significant stretchability properties. We printed three specimens for each of the developed inks. In Figure

2**d**, conductive electrode films could undergo stretchability up to approximately 100% of original length while piezoelectric films could be stretched to up to 30%. This means that the conductive and piezoelectric films present enough stretchability for the fabrication of flexible or stretchable devices.

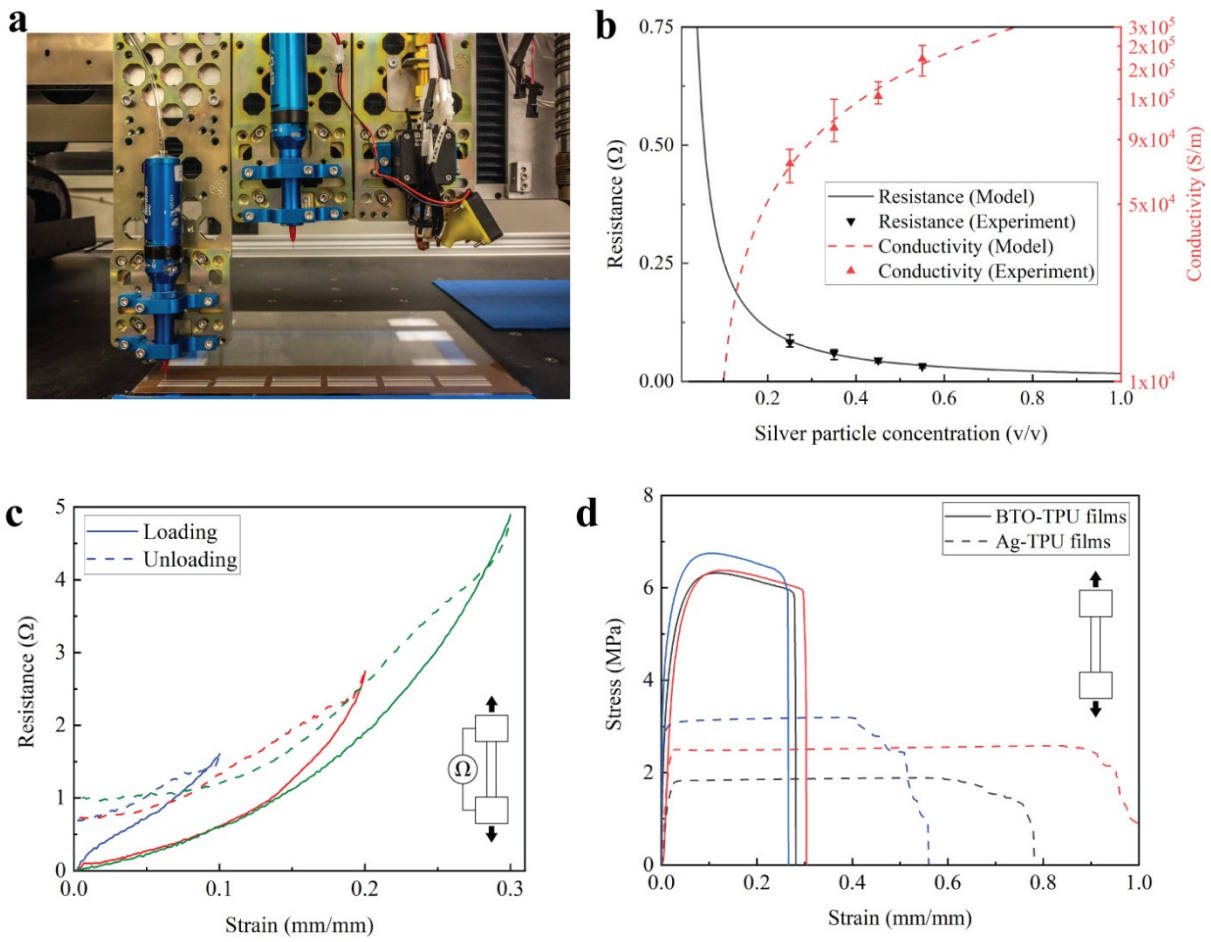

Figure 2. Characterization of inks and fabricated films: **a** Image of multi-material multi-process printing heads including two DIW and one FFF heads; the left DIW printing head is printing Ag-TPU ink through a 250 µm stainless steel nozzle (printed films have dimensions of 40 mm by 10 mm); **b** Electrical conductivity and resistivity of dried Ag-TPU composite films as a function of silver flake volume content. Lines are fit (triangle symbols); **c** Electrical

resistance of Ag-TPU during 10% (blue), 20% (red), and 30% (green) of strain; **d** Stress-strain curves for stretched printed conductive and piezoelectric films (three repetitions for each material).

Additive manufacturing of thermoplastic base layers. Thermoplastic filament made of polylactic acid (PLA) was inserted to FFF printing head to deposit the substrate material layer by layer to fabricate a 3D substrate.

Upon printing and drying of inks over the PLA substrate, piezoelectric and conductive electrodes with track widths of approximately 250 µm that contain a percolating network of BTO nano powders or silver flakes were achieved. Figure 3a depicts a Scanning Electron Microscopy (SEM) image of a printed silver film. Ag-TPU and BTO-TPU inks can develop a strong interface during printing. This strong interface might be due to the fact that both inks contain the same polymer matrix and solvents. Based on our vibration and bending results that will be discussed in the following section, this robust interface yields soft composite laminates that do not yield cracking or delamination during or after bending deformation. The co-solvent system being used in these ink formulations also helps to fuse the TPU ink to the PLA substrate. This adhesion is an important characteristic of these inks, since a common mode of failure in printed electronics is delamination of printed layers[28,29].

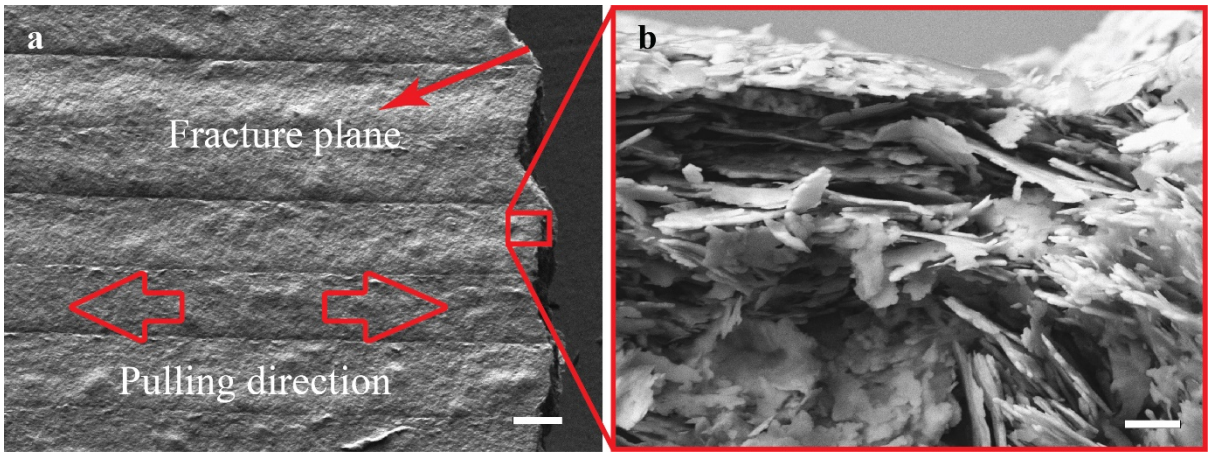

Figure 3. SEM images of a single layer Ag-TPU film after breaking (**a**) top view (scale bar=200 μm), (**b**) magnified cross-sectional view (scale bar=2 μm).

To explain the increase in resistivity of Ag-TPU films under stretching, we carried out SEM before and after stretching at different elongations to investigate their morphologies (Figure S3). From the SEM images of Figure S3, a permanent distorted TPU network-silver flake and the stretch of TPU matrix (e.g., at 30% strain in Figure S3b) can be seen. At a higher strain (e.g., 100% strain), electrical failure occurred the electrodes due to disconnection of the percolative TPU network-silver flake. Considering their low resistivity, minimum variation in resistance, and high stretchability, our Ag-TPU inks are stretchable conductors with good mechanical properties.

2.2 Fabrication of piezoelectric energy harvesting devices

Our developed materials and additive manufacturing platform performance was further demonstrated by 3D printing the stretchable conductive and piezoelectric inks into multilayer piezoelectric energy harvesting (PEH) devices with a planar or nonplanar PLA substrate as shown in Figure 4. Five devices namely called straight beam (SB), (ii) variable cross-section beam (VSB), (iii) S-shape beam (SSB), (iv) arc-beam (AB), and (v) semi-spherical shell (SSS) were 3D printed.

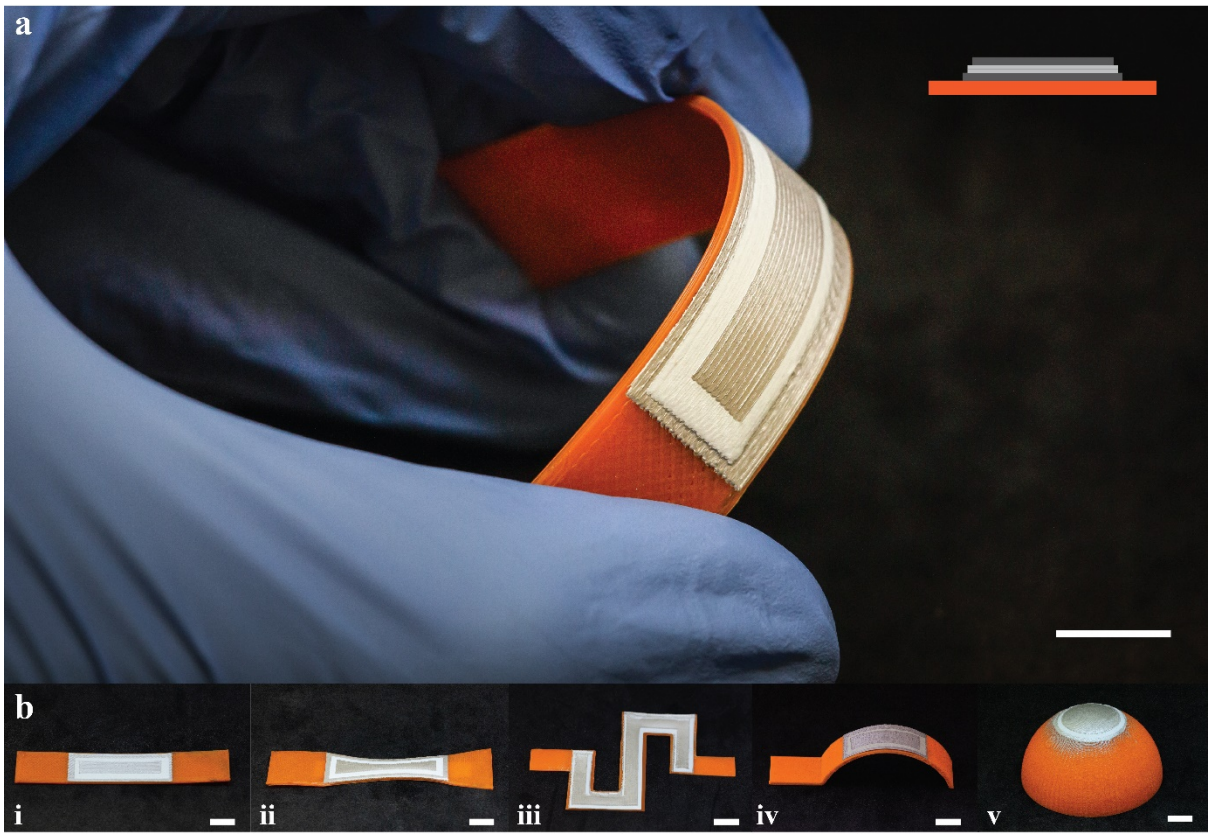

Figure 4. 3D printed flexible piezoelectric devices for monitoring or energy harvesting (scale bar = 10 mm): **a** Optical image of a flexible piezoelectric energy harvester under bending deformation; inset at the top right shows the schematic of the piezoelectric device with a PLA substrate (orange color) covered with conductive electrodes in grey color and piezoelectric layer in white color, **b** Piezoelectric energy harvesting demonstrators fabricated by multi-material multi-process additive manufacturing: (i) Straight beam (SB), (ii) variable cross-section beam (VSB), (iii) s-shape beam (SSB), (iv) arc-beam (AB), and (v) semi-spherical shell (SSS).

2.3 Piezoelectric poling

Poling is a necessary part of fabrication of piezoelectric devices. Molecular dipoles must be oriented in a single global direction within a structure. Electrical poling (Figure S4) is used for this molecular dipole orientation to obtain high electromechanical transformation. As

shown in Figure S4, we applied an electric field of 2kV to the sandwich structure in silicone oil medium at temperature of 80 °C. After cooling of the sample and removal of the poling electric field, most of the dipoles are locked into a configuration of near alignment known as the remnant polarization[30]

2.4 Vibration-based energy harvesting

To evaluate the piezoelectric energy harvesting performance, a free and forced vibration piezoelectric testing fixture was set up to extract the voltage data from the samples. A concentrated mass of 7.5g was added at a fixed distance from the clamped end (10 mm offset from the tip of the beams) of beam-type demonstrators shown in (Figure 4b i-iv). In the free vibration testing, cantilever beam samples had one end clamped and the other end displaced to 20 mm before release. In the forced vibration test, the input signals were generated using a function generator (in sine wave format), amplified at frequency of 10 Hz and applied at the clamped end of the beams. When PEH is under vibrational load by the electrodynamic shaker, an AC electrical signal is produced. Since direct current (DC) voltage is required for most electronic devices, an alternate current (AC) to DC full-bridge rectifier is required. Furthermore, a filtering capacitance is also required to smooth the rectified DC voltage (Figure 5). The voltage stored in the capacitor was measured by a digital multimeter (Fluke 87-V). The current and output were measured separately using an Electrometer (Keithley 6517b). The piezoelectric voltage was collected by a charge amplifier (Piezo Lab Amplifier, MEAS Specialties). The voltage data was then transferred to a Data Acquisition System (NI-9239) and both current and voltage data were processed separately in a LabVIEW program.

Figure S5 depicts a schematic of the forced vibration experimental setup. The set-up consists of a function generator (to generate a range of vibrational frequencies) and an amplifier

(to amplify the power of the signal generated by the function generator) and an electrodynamic shaker to provide a base excitation. The clamped end of all the cantilever demonstrators were attached to the electrodynamic shaker. The input signals were generated using a function generator (in sine wave format) at frequency of 10 Hz for samples shown in Figure 4b(i-iv).

The open circuit method is widely used for PEH [31]. This conventional interface circuit includes a simple AC-to-DC power converter. We measured both AC voltage and current AC outputs as well as DC voltage being stored in the capacitor. These results can be used to further investigate the effectiveness of the developed PEH devices and their output power. The AC voltage and current responses of demonstrators under forced vibration scheme are shown in Figure 5 and Figure 6. Figure 5 shows the voltage outputs measured for the four PEH devices SB, VSB, SSB, AB with the induced open-circuit voltages of ~2.7, 0.72, 0.25, and 0.80 V_{pp} (peak to peak voltage) at the 10g base excitation and 10 Hz frequency, respectively. Maximum voltage or power output in a resonant system such a PEH happens when ambient vibration frequency is matched with PEH resonant frequency. If these frequencies are not matched, a significant drop in the output (voltage and power) can be obtained. Therefore, to achieve the maximum energy harvesting from each of the demonstrators, the input frequency and the tip mass must be chosen to tune the resonance frequency of their corresponding demonstrator. In this work, for sake of simplicity, the input excitation frequency and the tip mass were considered constant values for all the forced vibration demonstrators. For the chosen input frequency and the tip mass, the demonstrators that their resonance frequency are closer to the excitation frequency exhibit higher output voltage.

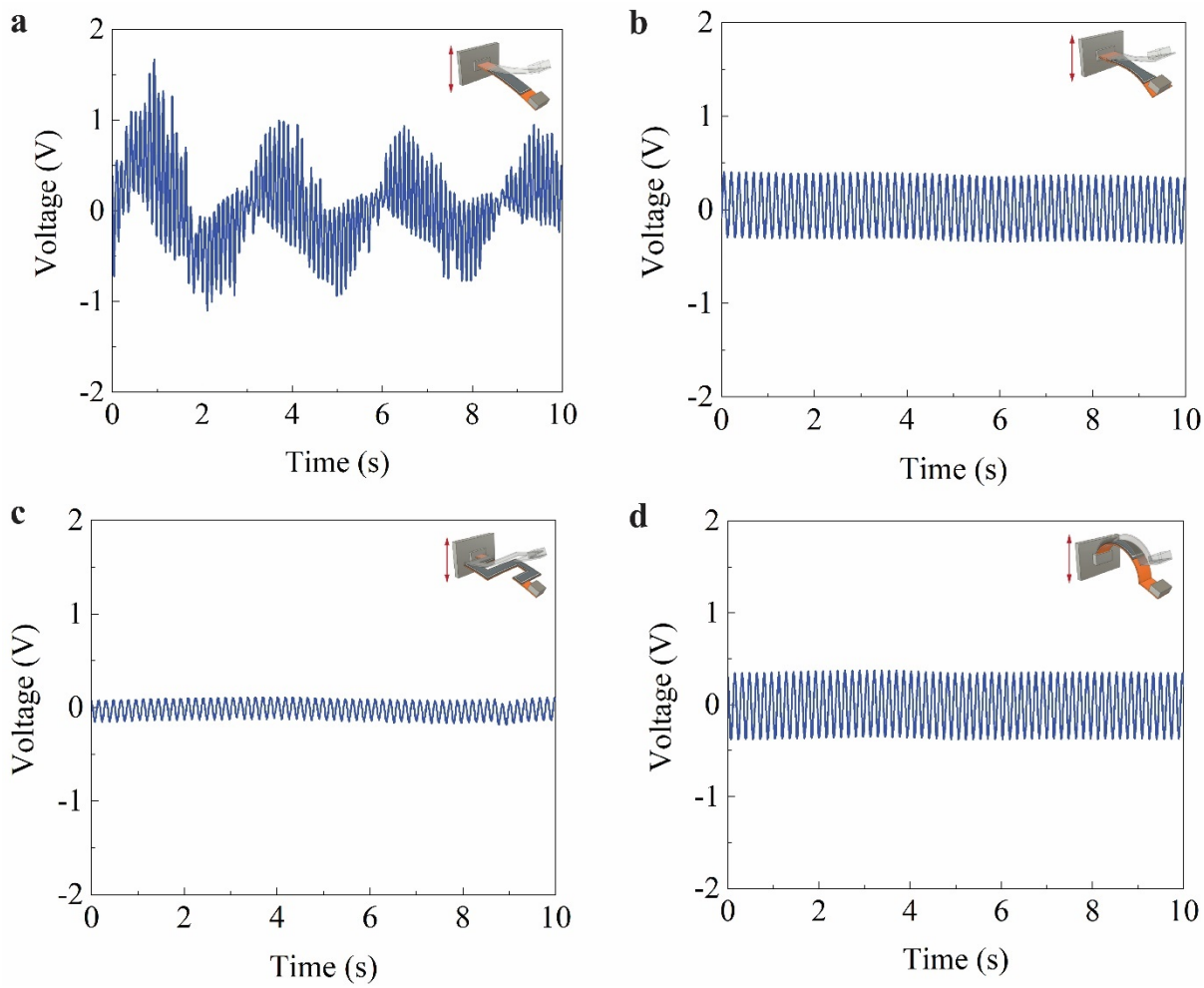

Figure 5. The open circuit voltage measured when PEH devices were under forced vibration: **a** SB, **b** VSB, **c** SSB, and **d** AB. For the given input frequency and the tip mass, SB exhibits higher output voltage due to its resonance frequency closer to the excitation frequency.

A similar interpretation is valid to electrical current results. Figure 6 shows the electrical current time history for SB, VSB, SSB, AB PEH devices. These devices were tested under the same condition with voltage results in a separate time. The scale of electric current values is in the range of sub 100 nA. This matches with our expectations and similar works in the literature[5,32]. From Figure 6, the SB produced a maximum peak current of 35 nA, which is much higher than the other three types of harvesters. Similar to the case of voltage results, the higher current values are associated with the device with excitation frequency to be near its

resonance frequency. In this case, given the base excitation of 10g and frequency of 10 Hz, SB has the resonance frequency closer to the input frequency of 10 Hz.

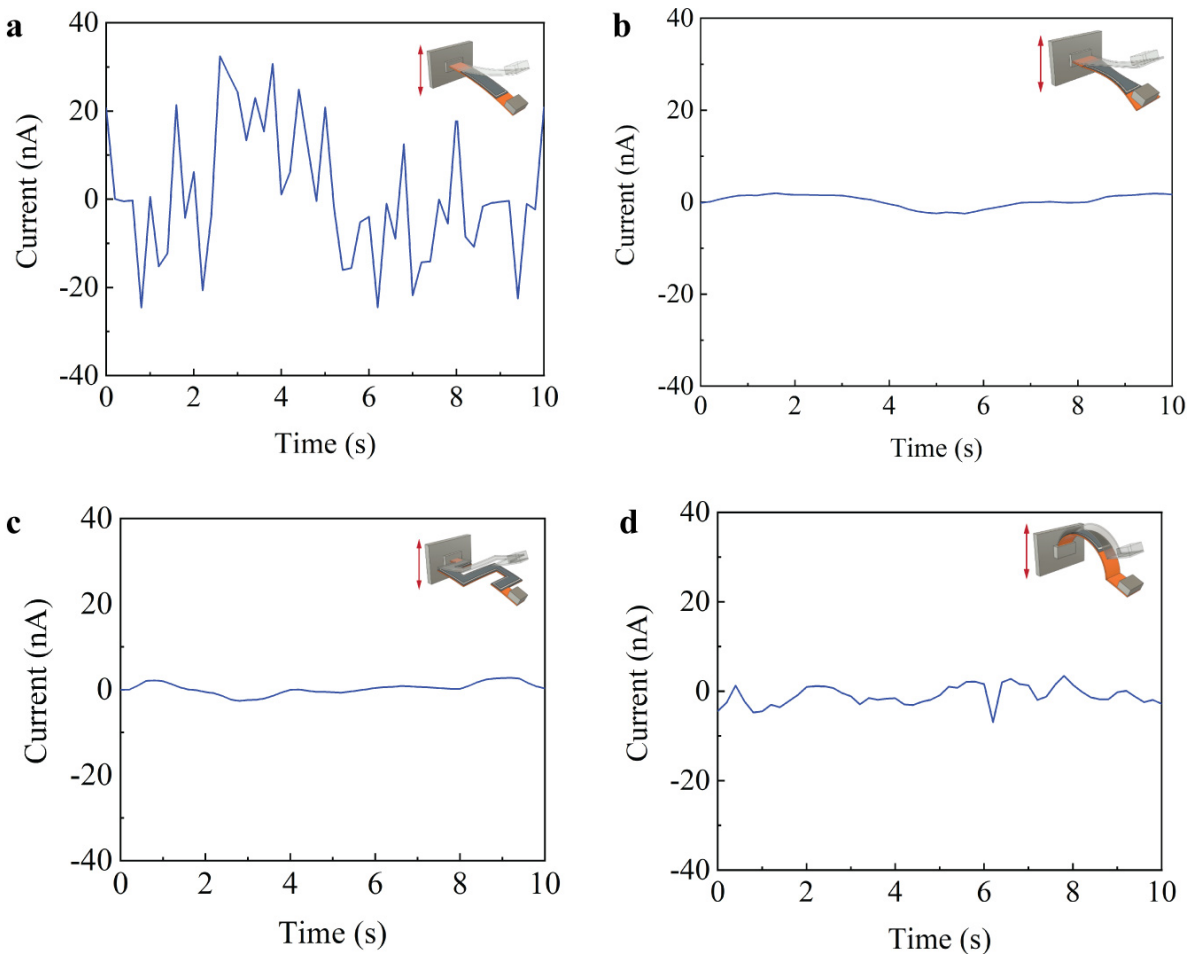

Figure 6. The open circuit current measured when PEH devices were under forced vibration (10g base excitation at 10 Hz): **a** SB, **b** VSB, **c** SSB, and **d** AB. SB exhibits the highest output current due to its resonance frequency closer to the excitation frequency.

To verify the performance of PEHs for energy storage, we carried out experiments using the 3D printed demonstrators in forced vibration tests to charge a capacitor (100 μF). The experimental data from the charging process of the capacitor was recorded by a digital multimeter, as shown in Figure 7. The capacitor voltage time history is illustrated in Figure 7,

where we see the 3D printed PEHs can charge the 100 μF capacitor to, for example, 3 mV, within 11, 27, 67, 78 and 150 s by SB, VSB, SSB, AB and SSS, respectively.

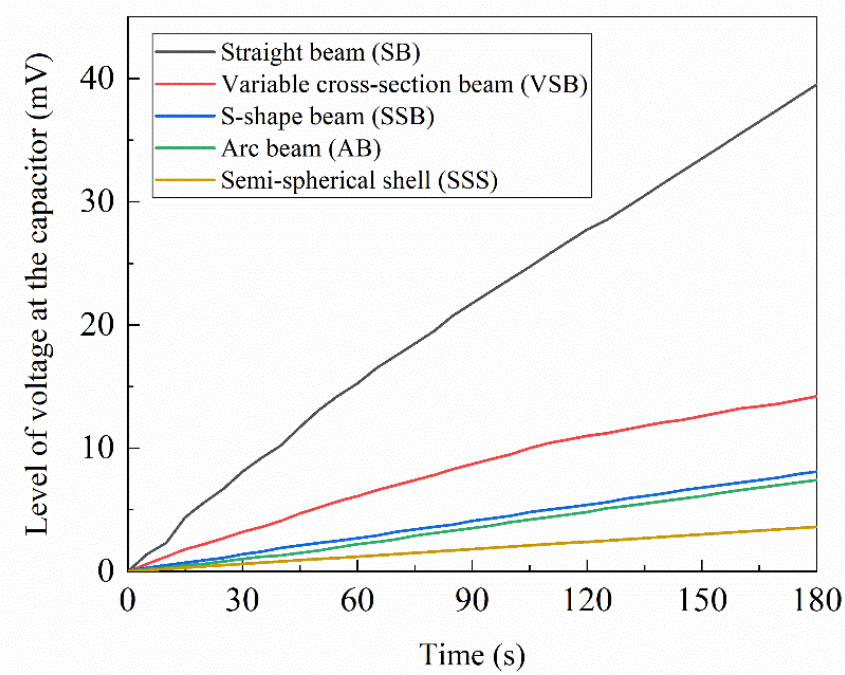

Figure 7. Capacitor voltage data for PEHs recorded during forced vibration test

In the free vibration test, cantilever beam specimens were fixed at one end and the other end with tip mass was manually deflected to 20 mm displacement by index finger before release. The resulting voltage response was continuously recorded using the same equipment described in forced vibration test. Figure 8 shows the first 10s free vibration time history of the four demonstrators under the same initial displacement. Demonstrators SB, VSB, and AB were subjected to three sequences of free vibration test, and SSB, due to its spherical shape and limitation for cantilever setup, were subjected to one release of initial lateral displacement. In free vibration mode, the given initial displacement of 20 mm to the tip of cantilevers (that carry tip mass) induces a frequency that is closer to the first resonance frequency of SB demonstrator. The difference in geometry of PEHs makes the amount of stress that is being transferred from

initial displacement to piezoelectric layers vary from one configuration to another. Therefore, we expected different response from the PEHs.

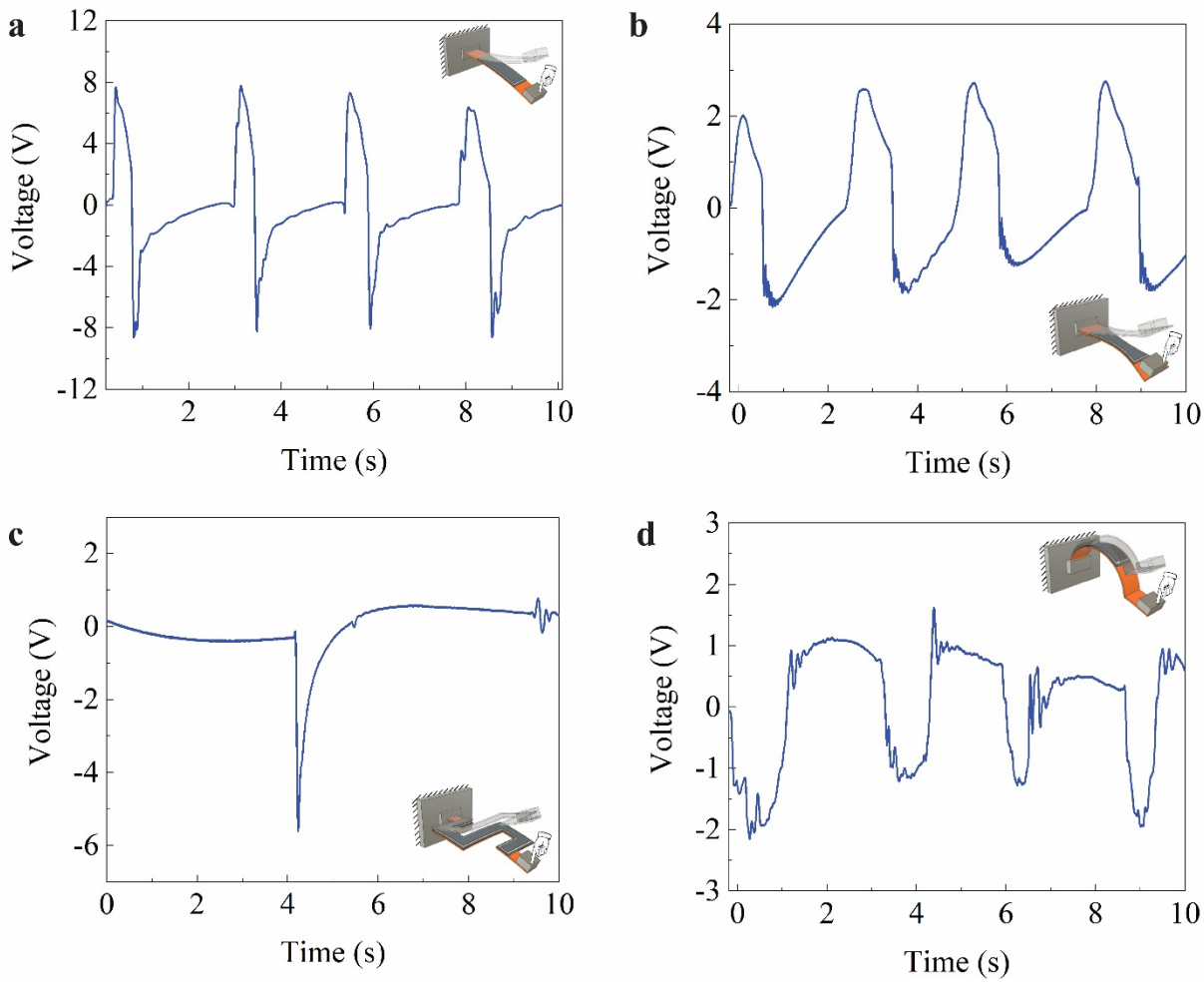

Figure 8. The open circuit time history of voltage measured when PEH devices were under free vibration test: **a** SB, **b** VSB, **c** SSB, and **d** AB. SB exhibits the highest output current due to its resonance frequency closer to the tip excitation.

Figure 9 shows the schematic as well as the output voltage and electric current for SSS PEH. The vibration and current results were measured when SSS was under lateral load. The lateral compressive load was applied by holding the demonstrator in hand and imposing

approximately 20 mm initial displacement (Figure 9a) with approximately two seconds interval. This process was performed three time in a row. Figure 9b-c show the measured voltage and current responses of the SSS PEH with the induced open-circuit voltage of ~15 V_{pp} and the induced open-circuit maximum current of 6 nA.

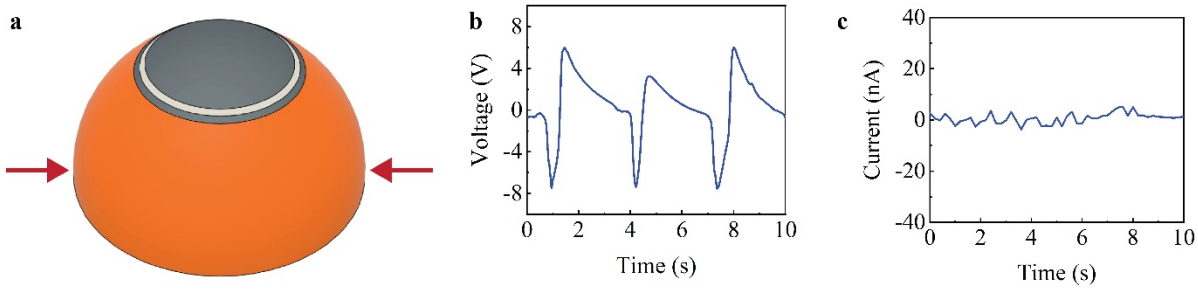

Figure 9. **a** Schematic of SSS (diameter = 50 mm, wall thickness = 1 mm) under lateral compressive load; the open circuit time history of voltage and current measured when SSS was under free vibration test: **b** voltage, and **c** current.

In summary, we demonstrated new piezoelectric and conductive inks for multimaterial multiprocess planar and nonplanar AM of piezoelectric devices. We developed convenient, less toxic, and inexpensive formulations for fabrication of highly stretchable conductive and piezoelectric inks for DIW. The highly conductive and stretchable electrode with a high conductivity of ~1.87 $\times 10^5$ S/m was successfully prepared using a printable silver flake-embedded TPU ink. The stretchable piezoelectric ink also showed effective performance in converting mechanical strain to electric charges. The proposed advanced technology utilized in AM of PEHs can be applied for the rapid production of energy harvesters. Importantly, the broad set of printable inks (inks made of polymer modified with either ceramics or metal particles) combined with planar and nonplanar AM, offers a chance to enhance the functionality of parts made by AM (e.g., in areas such as electronics, aerospace, robotics, and textile) via this multi-material multi-process manufacturing platform.

3. Methods

Materials: The stock material used as a substrate to build the PEH devices is a PLA filament (1.75 mm diameter). We dissolved TPU (85A) in DMF (N,N-dimethylformamide, Sigma Aldrich) at 1:2 DMF by weight (wt./wt.) to prepare TPU ink.

For production of the conductive ink, silver flakes, (Inframat Advanced Materials) with purity of 99.95% and average particle size of 2–5 μm) were added to TPU ink at 70% by weight. Acetone (Sigma-Aldrich) was then added at ratio of 1 TPU:2 Acetone by weight. The mixture was ball milled for 20 min and transferred into syringes (3 cc), centrifuged at 1500rpm for 1 hour for air bubbles removal.

$BaTiO_3$ (Inframat Advanced Materials) were added to TPU ink at 40% by weight and then Acetone (Sigma-Aldrich) was added at weight ratio 1 TPU:2 acetone. The mixture was ball milled for 20 min. After mixing, another dosage of Acetone at weight ratio 1 TPU:2 Acetone was added to lower the viscosity and the mixture was ball milled for another 20 min. The final mixture was degassed through a two step-process. In the first step, the mixture was degassed in a vacuum degassing chamber for 5 min, then transferred into 3 cc syringes, centrifuged (to remove air bubbles) at 1500 rpm for 1 hour.

Viscosity characterization: The viscosity of all TPU, Ag-TPU and BTO-TPU inks were measured under standard room conditions using a controlled stress rheometer (MCR 502, Anton Paar) equipped with parallel plates (shear rates varied from 0.001 to 100 s^{-1}).

Electromechanical characterization: Single layer Ag-TPU thin rectangular films (4 cm × 1 cm) were 3D printed. Once dried, the thickness of each sample was measured. Printed Ag-TPU films were mounted to a tensile machine (Model 50 EL, MTS Insight) and connected to a resistance measuring card (four-point method, PCI-4070 card, National Instruments) for simultaneous electromechanical characterization. Tensile tests were performed at 40 mm s^{-1}.

Planar and nonplanar 3D printing: 3D Printing was performed with a motion control system (ABG10000 model, Aerotech Inc., Pittsburgh, PA, USA) with four independent z-axes (see Video S1-3). Two heads were assigned for DIW (conductive and piezoelectric inks) and one head was assigned for FFF (PLA substrate). For the case of planar AM, print paths were initially generated with Simplify3D slicing software and then translated to Aerobasic language (the language of Aerotech custom-made 3D printer) using offline robotic simulation software RoboDK. In the case of nonplanar AM, the generated print paths (by Simplify3D) were projected on the surface of a cylinder or sphere using mathematical package MATLAB and then translated for gantry system using RoboDK for fabrication of AB and SSS. Extrusion of inks (via air pressure) was performed with a custom controller (MËKANIK) using 250 μm cylindrical dispense tips (EFD) for both conductive Ag-TPU and piezoelectric BTO-TPU inks with printing speed of 10 mm/s. After printing each layer, the part is left at room temperature for evaporation of solvents (~60 seconds) before printing the consequent layers. The average dried thickness of each DIW layer is 200 μm. For printing substrate, FFF process parameters such as layer thickness, feed rate, or temperature were fixed for all the devices and are shown in Table S. 1.

Poling process: The samples were placed inside an oil bath on a planar copper electrode connected to a high-voltage power supply (ES60, 10W negative, Gamma High Voltage Research, Inc.) and poled under 2 kV at 80°C for 1 h. The samples were then cooled down to

room temperature before removing the electric field to avoid the misalignment of dipole moments.

References

[1] M. Rafiee, R. D. Farahani, D. Therriault, *Adv. Sci.* **2020**, *7*, 1902307.

[2] O. D. Yirmibesoglu, L. E. Simonsen, R. Manson, J. Davidson, K. Healy, Y. Menguc, T. Wallin, *Commun. Mater.* **2021**, *2*, DOI 10.1038/s43246-021-00186-3.

[3] H. Yuk, B. Lu, S. Lin, K. Qu, J. Xu, J. Luo, X. Zhao, *Nat. Commun.* **2020**, *11*, 4.

[4] M. A. Skylar-Scott, J. Mueller, C. W. Visser, J. A. Lewis, *Nature* **2019**, *575*, 330.

[5] M. Safaei, H. A. Sodano, S. R. Anton, *Smart Mater. Struct.* **2019**, *28*, DOI 10.1088/1361-665X/ab36e4.

[6] M. Rafiee, X. Q. He, S. Mareishi, K. M. Liew, *Int. J. Appl. Mech.* **2015**, *7*, DOI 10.1142/S175882511550074X.

[7] M. Rafiee, X. Q. He, K. M. Liew, *Smart Mater. Struct.* **2014**, *23*, 065001.

[8] Z. Wang, X. Yuan, J. Yang, Y. Huan, X. Gao, Z. Li, H. Wang, S. Dong, *Nano Energy* **2020**, *73*, 104737.

[9] S. Bodkhe, G. Turcot, F. P. Gosselin, D. Therriault, *ACS Appl. Mater. Interfaces* **2017**, *9*, 20833.

[10] H. Kim, A. Renteria-Marquez, M. D. Islam, L. A. Chavez, C. A. Garcia Rosales, M. A. Ahsan, T. L. B. Tseng, N. D. Love, Y. Lin, *J. Am. Ceram. Soc.* **2019**, *102*, 3685.

[11] Y. Jin, N. Chen, Y. Li, Q. Wang, *RSC Adv.* **2020**, *10*, 20405.

[12] W. Wang, J. Sun, B. Guo, X. Chen, K. P. Ananth, J. Bai, *J. Eur. Ceram. Soc.* **2020**, *40*, 682.

[13] N. Godard, S. Glinšek, A. Matavž, V. Bobnar, E. Defay, *Adv. Mater. Technol.* **2019**, *4*,

1.

[14] E. R. Cholleti, *IOP Conf. Ser. Mater. Sci. Eng.* **2018**, *455*, DOI 10.1088/1757-899X/455/1/012046.

[15] S. Bodkhe, P. Ermanni, *Multifunct. Mater.* **2019**, *2*, 022001.

[16] A. C. Siegel, S. T. Phillips, M. D. Dickey, N. Lu, Z. Suo, G. M. Whitesides, *Adv. Funct. Mater.* **2010**, *20*, 28.

[17] X. Zhou, K. Parida, O. Halevi, Y. Liu, J. Xiong, S. Magdassi, P. S. Lee, *Nano Energy* **2020**, *72*, 104676.

[18] A. D. Valentine, T. A. Busbee, J. W. Boley, J. R. Raney, A. Chortos, A. Kotikian, J. D. Berrigan, M. F. Durstock, J. A. Lewis, *Adv. Mater.* **2017**, *29*, 1.

[19] T. Zhong, N. Jin, W. Yuan, C. Zhou, W. Gu, Z. Cui, *Materials (Basel).* **2019**, *12*, 1.

[20] L. Cai, S. Zhang, Y. Zhang, J. Li, J. Miao, Q. Wang, Z. Yu, C. Wang, *Adv. Mater. Technol.* **2018**, *3*, 1700232.

[21] H. He, M. Akbari, L. Sydanheimo, L. Ukkonen, J. Virkki, in *2017 Int. Symp. Antennas Propagation, ISAP 2017*, **2017**.

[22] S. Gonçalves, J. Serrado-Nunes, J. Oliveira, N. Pereira, L. Hilliou, C. M. Costa, S. Lanceros-Méndez, *ACS Appl. Electron. Mater.* **2019**, *1*, 1678.

[23] J. H. Lee, K. Y. Lee, M. K. Gupta, T. Y. Kim, D. Y. Lee, J. Oh, C. Ryu, W. J. Yoo, C. Y. Kang, S. J. Yoon, J. B. Yoo, S. W. Kim, *Adv. Mater.* **2014**, *26*, 765.

[24] Y. Li, B. Li, J. Sun, K. Cai, J. Zhou, L. Li, *Key Eng. Mater.* **2012**, *512–515*, 390.

[25] H. Kim, F. Torres, D. Villagran, C. Stewart, Y. Lin, T. L. B. Tseng, *Macromol. Mater. Eng.* **2017**, *302*, 1.

[26] A. M'Barki, L. Bocquet, A. Stevenson, *Sci. Rep.* **2017**, *7*, 1.

[27] H. J. Qi, M. C. Boyce, *Mech. Mater.* **2005**, *37*, 817.

[28] N. Matsuhisa, M. Kaltenbrunner, T. Yokota, H. Jinno, K. Kuribara, T. Sekitani, T. Someya, *Nat. Commun.* **2015**, *6*, 7461.

[29] K. Fukuda, K. Hikichi, T. Sekine, Y. Takeda, T. Minamiki, D. Kumaki, S. Tokito, *Sci. Rep.* **2013**, *3*, 2048.

[30] M. D. Nguyen, E. Houwman, M. Dekkers, H. N. Vu, G. Rijnders, *Sci. Adv. Mater.* **2014**, *6*, 243.

[31] N. Kawai, Y. Kushino, H. Koizumi, *IECON 2015 - 41st Annu. Conf. IEEE Ind. Electron. Soc.* **2015**, 1121.

[32] X. Yuan, X. Gao, J. Yang, X. Shen, Z. Li, S. You, Z. Wang, S. Dong, *Energy Environ. Sci.* **2020**, *13*, 152.

Acknowledgement

The financial support from National Science and Engineering Research Council (NSERC, Grant # RGPIN-2018-04566), the Department of National Defence (DND) (Grant#: DGDND-2018-00011) are acknowledged by the authors. The first author also acknowledges Postdoctoral Scholarship from the Fonds de Recherche du Québec – Nature et Technologies (FRQNT). The authors would also like to acknowledge the technical supports from Mr. Y. Landry-Ducharme, and Drs. R. D. Farahani, and K. Chizari.

Author contributions

M.R. conceptualized, designed the Ag-TPU and BTO-TPU inks and fabricated the materials and devices, poled the piezoelectric samples, characterized the piezoelectric energy harvesting devices, contributed to the 3D schematic and illustration and wrote the original draft. F.G. contributed to preparation Ag-TPU and BTO-TPU inks, carried out electrical conductivity/resistivity, SEM imaging and tensile characterizations. R.T. contributed to poling and PEH characterization. A.B. contributed to programming of gantry system and interpretation of gcode for Aerotech gantry system. G.C. modeled the geometries and prepared the STL files, and contributed to the 3D schematics and illustrations. D.T. supervised the project, performed the project administration, and funding acquisition. All authors contributed to reviewing the writing.

Supporting Information

Mohammad Rafiee, Floriane Granier, Rui Tao, Abraham Bhérer-Constant, Gabriel Chenier and Daniel Therriault

Multi-material multi-process planar and nonplanar additive manufacturing of piezoelectric devices

Figure S1. A photograph of Aerotech (ABG10000 model, Aerotech Inc., USA) gantry motion control system. The print bed sits on the x-y motion stage while all printing heads are mounted on the z-direction stages. The machine has a build area of 0.4m x 0.4m , with local accuracy, repeatability, and maximum velocity ±2 µm, ±0.3 µm, and 120 mm/s, respectively. Each z-axis printhead has 0.15 m of vertical travel, with accuracy, repeatability, and maximum velocity of ±0.75 µm, ±0.3 µm, and 50 mm/s, respectively.

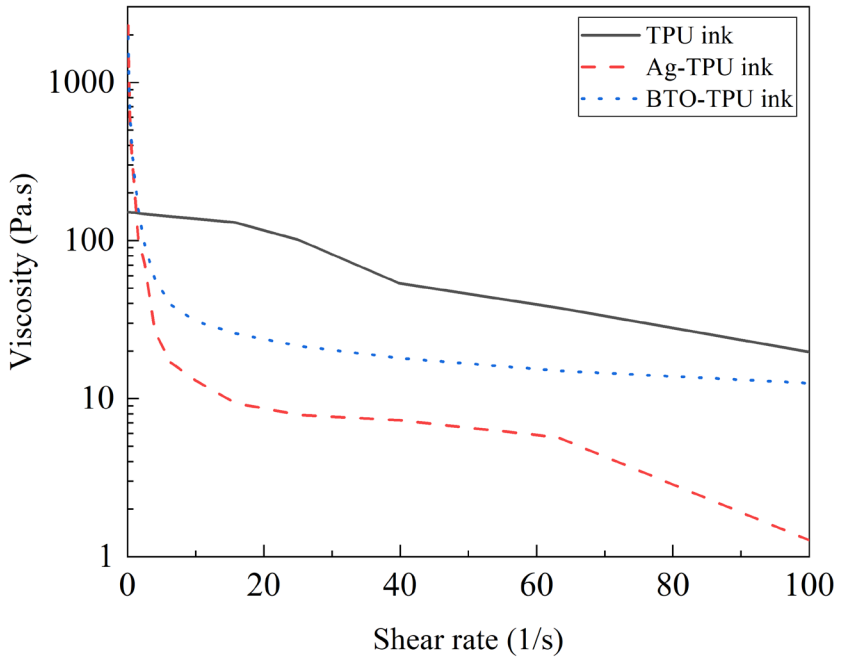

Figure S2. Viscosity of inks (TPU, Ag-TPU and BTO-TPU) as a function of shear rate

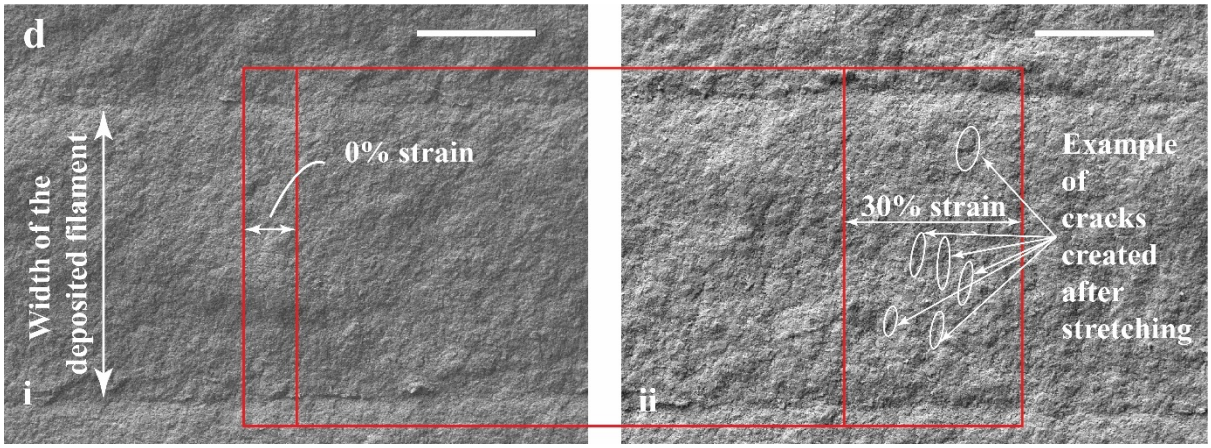

Figure S3. SEM image of a single-layer Ag-TPU filament (top surface) (scale bar = 100 μm) under (a) 0% strain and (b) 30% strain.

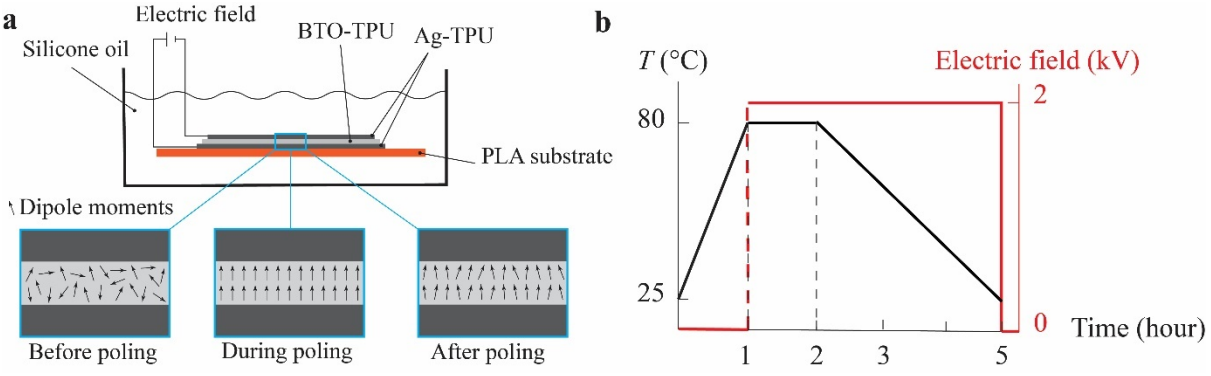

Figure S4. Poling of 3D printed PEH devices: **a** Schematic of contact poling process for a PEH in a silicone oil bath with top and bottom electrodes with bottom insets showing the orientation of dipole moments before, during and after poling; **b** Time-temperature scheme of the DC-electric field poling process.

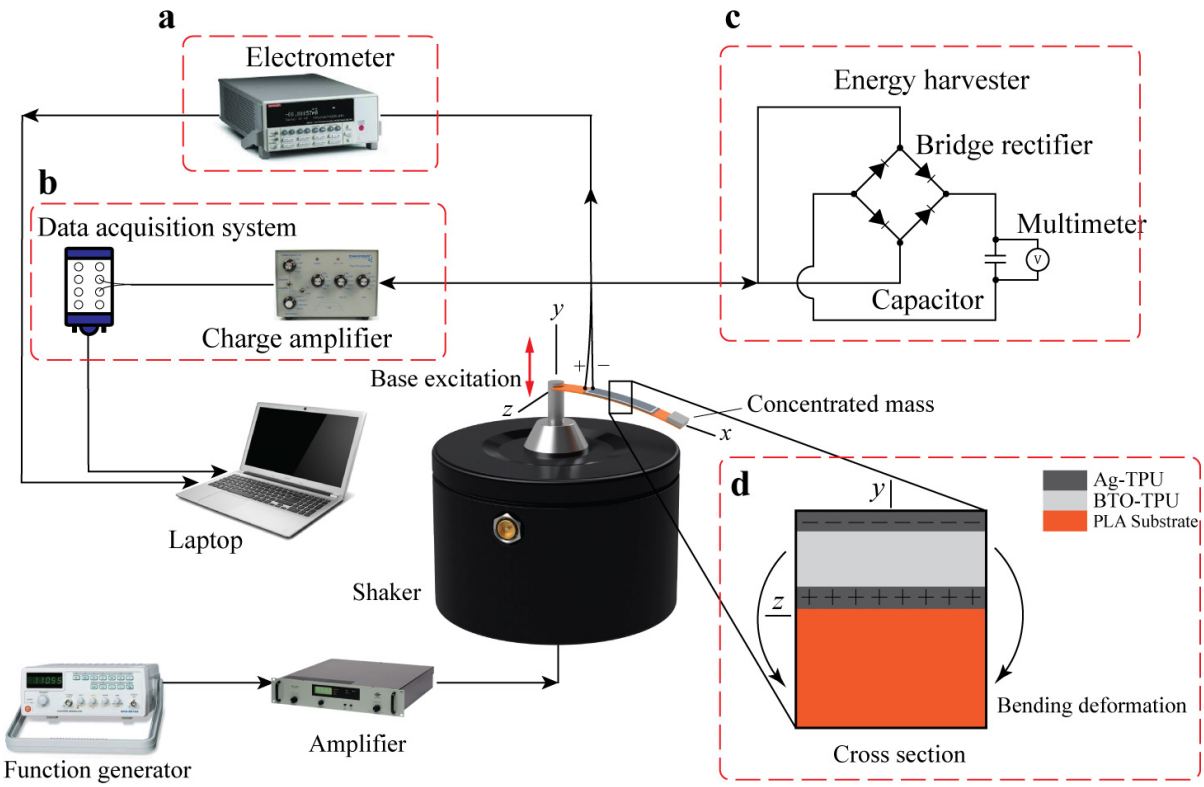

Figure S5. Schematic of the forced vibration experimental setup. **a** An electrometer was used to measure the output current from the PEH and **b** a charge amplifier to capture the voltage and transfer to the DAQ and process it in the LabVIEW software. **c** A PEH circuit was also used for rectifying and smoothing the AC voltage and energy storage in the capacitor. **d** Schematic of a representative 3D printed PEH device under base excitation that causes bending deformation with an inset showing the material composition and electric charge generation throughout the cross-section of the device.

Table S. 1. Process parameters and their levels used in this work

Parameters	**Value**
Layer thickness (mm)	0.2
Feed rate (mm/s)	50
Flow rate (mm^3/s)	4.8
Nozzle temperature (°C)	210
Nozzle size (mm)	0.4